

Nonlinear magnetotransport in a two-dimensional system with merging Dirac points

Ojasvi Pal¹, Bashab Dey^{1,2} and Tarun Kanti Ghosh¹

¹Department of Physics, Indian Institute of Technology-Kanpur, Kanpur-208016, India

²Institute for Theoretical Physics, University of Regensburg, Regensburg-93053, Germany

We study linear and second-order nonlinear (NL) transport properties of a two-dimensional gapped semi-Dirac system with merging Dirac nodes in the presence of a low magnetic field (B) using semi-classical Boltzmann transport formalism. The resulting dispersion at the merging point exhibits semi-Dirac behavior which is quadratic in the x -direction and linear in the y -direction. We find that the combined effects of the intrinsic anisotropic spectrum, Berry curvature and orbital magnetic moment (OMM) lead to finite NL conductivities in the system. We obtain exact analytical expressions of linear and second-order NL conductivities which allow us to analyze their dependence on Fermi energy and system gap parameter δ_0 . The topology of the Fermi surface for $\delta_0 > 0$ changes from two disjoint Fermi contours to a single one across a saddle point as the Fermi energy is increased. This feature is reflected in the nature of obtained conductivities through a kink in their variations with Fermi energy. We find that the geometric mean (ratio) of Drude conductivities along the x and y directions is independent of δ_0 for low (high) doping. Interestingly, we show that the ratio of the anomalous velocity and Lorentz force-induced NL Hall conductivity to the NL anomalous Hall conductivity is independent of δ_0 and inversely related to Fermi energy only. For current along the x -direction, the NL longitudinal and Hall resistivities show B -linear and B^0 dependences respectively in the lowest order of B . However, for current along the y -direction, the longitudinal NL resistivity has no contribution in both zeroth and linear order of B while the NL Hall resistivity is B -linear. The anisotropy in the nature of B -dependencies of the NL resistivities may be experimentally relevant signatures of band geometric quantities and merging Dirac nodes in such systems.

I. INTRODUCTION

The exfoliation of graphene in 2004 marked an important epoch in the history of 2D materials due to its unique linear-Dirac spectrum and exotic transport properties^{1,2}. The two subbands of graphene touch at two inequivalent points in the reciprocal space named Dirac points, effectively describing the low-energy properties. These Dirac points can be manipulated by varying band parameters such as interaction strength and hopping amplitudes which results in the motion of Dirac points. Other two-dimensional physical systems with such spectrum have been observed in organic conductor α -(BEDT-TTF)₂I₃ under pressure³⁻⁶, 8-*Pmmn* borophene^{7,8}, artificially fabricated nanostructures^{9,10} and ultracold atoms^{13,14}.

Several studies discovered the merging of Dirac points in the electronic spectrum of two-dimensional systems^{15,16}. The merging of a pair of Dirac points into a single one shows the existence of a topological Lifshitz transition which marks the separation between the semimetallic phase with two disconnected Fermi surfaces and an insulating gapped phase. This also leads to special semi-Dirac dispersion hosting massive fermion behavior along one direction while massless Dirac characteristics in the orthogonal direction^{17,18}. It has been predicted that materials like TiO₂/VO₂ nanostructures under quantum confinement¹⁹ and dielectric photonic crystals²⁰ can exhibit such low-energy dispersions. Recently experimental realizations were also observed in optical lattices²¹ and microwave cavities¹¹. The transport properties such as diffusion²², optical conductivity²³⁻²⁶, formation of Landau levels spectra un-

der magnetic field^{27,28}, magneto-optical conductivity²⁹, dynamic polarization and plasmons³⁰ has been studied extensively for semi-Dirac systems. The Landau levels and transport properties for a semi-Dirac nanoribbon were discussed in recent work³¹. Very recent studies probed the topological phases of a Chern insulator in such systems by tuning the strength of a circularly polarized light³² and in the presence of extended range hopping³³.

The topological behavior of the bands is manifested in the Berry curvature and OMM of the electrons which can significantly affect the linear and the nonlinear transport properties³⁴. Some well-known examples in the linear response regime are anomalous Hall effect³⁵⁻³⁷, anomalous thermal Hall effect^{38,39}, planar Hall effect^{40,41}, magnetoresistance^{42,43}. The discovery of the nonlinear anomalous Hall effect induced by the Berry curvature dipole⁴⁴ in the time-reversal symmetric (TRS) system accelerated the investigation of other NL transport phenomena⁴⁵⁻⁵³. Moreover, it has been realized that such NL transport responses in 2D Dirac systems survive either in the presence of spin-orbit coupling which results in tilting of the Dirac cone, or higher order warping of the Fermi surface^{44,54}. Recent studies reveal that the low-energy Hamiltonian that features a pair of Dirac points separated by a saddle point or the merging of two Dirac points can give rise to Berry curvature dipole induced NL transport properties⁵⁵. However, the linear and nonlinear current responses of such systems in the presence of a magnetic field are not explored.

In this work, we calculate the contribution of Berry curvature and OMM to the linear and nonlinear conductivities in the presence of a weak magnetic field, using the

Boltzmann approach. We also study the second-order NL magnetoresistivity of the system for two different orientations of the applied current. The anisotropy in the nature of B -dependencies of the NL resistivities may act as an experimental probe for band geometric quantities as well as merging Dirac nodes in these systems.

This paper is structured as follows: In Sec. II, we present the general formulas to calculate the linear and second-order nonlinear current responses in the presence of a weak magnetic field. In particular, we discuss the contribution of Berry curvature and OMM to the linear and nonlinear magnetoconductivities. In Sec. III, we apply the described approach to 2D gapped semi-Dirac model with merging Dirac nodes and calculate its linear and nonlinear magnetoconductivities. We further analyze our results and discuss the dependence of all the contributions on Fermi energy and other system parameters in its subsequent subsections. Section IV is dedicated to the discussion of the obtained linear and nonlinear magnetoresistivities. Finally, we summarize our main results in Sec. V

II. THEORETICAL FORMULATION

In this section, we provide the general formalism to calculate the linear and second-order nonlinear current responses in presence of the electric field which oscillates in time but uniform in space, $\mathbf{E}(t) = \mathbf{E}e^{i\omega t} + \mathbf{E}^*e^{-i\omega t}$ and a static magnetic field \mathbf{B} . Theoretically, for an applied electric field $\mathbf{E}(t)$, the linear current of fundamental frequency $j_a^\omega = \sigma_{ab}E_b$ and the nonlinear current $j_a^{\text{NL}} = \text{Re}[j_a^{(0)} + j_a^{(2\omega)}e^{i\omega t}]$ are measured. Here, $j_a^{(0)} = \sigma_{abc}^{(0)}E_bE_c^*$ describes the NL DC current and $j_a^{(2\omega)} = \sigma_{abc}^{(2\omega)}E_bE_c$ describes the second harmonic current with $E \in \mathbb{C}$ and a, b and c represent the coordinate indices. The charge current is defined as $\mathbf{j}(t) = -e \int [d\mathbf{k}] D_{\mathbf{k}}(\mathbf{r}) f(t)$, where $[d\mathbf{k}] = d^2k/(2\pi)^2$ and $f(t)$ represents the nonequilibrium distribution function (NDF) which is discussed later in this section.

The modified semiclassical equations of motion (including Berry curvature and OMM) for the configuration ($\mathbf{E} \perp \mathbf{B}$) are given by^{34,56,57}

$$\dot{\mathbf{r}} = \frac{1}{D} \left[\tilde{\mathbf{v}}_{\mathbf{k}} + \frac{e}{\hbar} (\mathbf{E}(t) \times \boldsymbol{\Omega}) \right], \quad (1)$$

$$\hbar \dot{\mathbf{k}} = \frac{1}{D} \left[-e\mathbf{E}(t) - e(\tilde{\mathbf{v}}_{\mathbf{k}} \times \mathbf{B}) \right], \quad (2)$$

Here, $\boldsymbol{\Omega}$ is the Berry curvature and $D = [1 + (e/\hbar)(\mathbf{B} \cdot \boldsymbol{\Omega})]$ is the phase space factor which modifies the phase space volume for the Berry curvature connected dynamics as $[d\mathbf{k}] = D^{-1}[d\mathbf{k}]$. The semiclassical band velocity is defined as $\hbar \tilde{\mathbf{v}}_{\mathbf{k}} = \nabla_{\mathbf{k}} \tilde{\epsilon}_{\mathbf{k}}$, where $\tilde{\epsilon}_{\mathbf{k}} = \epsilon_{\mathbf{k}} - \epsilon_{\mathbf{k}}^m$ is the modified band energy due to Zeeman-like coupling of OMM with the external magnetic field. The OMM modified velocity

can be expressed as $\tilde{\mathbf{v}}_{\mathbf{k}} = \mathbf{v}_{\mathbf{k}} - \mathbf{v}_{\mathbf{k}}^m$ with $\hbar \mathbf{v}_{\mathbf{k}}^m = \nabla_{\mathbf{k}}(\mathbf{m} \cdot \mathbf{B})$. The Berry curvature of the n -th band of the Hamiltonian H can be computed using^{34,58}

$$\Omega_a^n = -2\varepsilon_{abc} \sum_{n \neq n'} \frac{\text{Im}[\langle n | \partial_{k_b} H | n' \rangle \langle n' | \partial_{k_c} H | n \rangle]}{(\epsilon_n - \epsilon_{n'})^2}. \quad (3)$$

Here, ε_{abc} is the Levi-Civita symbol and $abc \in xyz$. The orbital magnetic moment which is generated by the semi-classical self-rotation of the Bloch wave packet can be found as⁵⁹

$$m_a^n = -\frac{e}{\hbar} \varepsilon_{abc} \sum_{n \neq n'} \frac{\text{Im}[\langle n | \partial_{k_b} H | n' \rangle \langle n' | \partial_{k_c} H | n \rangle]}{(\epsilon_n - \epsilon_{n'})}. \quad (4)$$

The Boltzmann transport equation within the relaxation time approximation to obtain the non-equilibrium distribution function (NDF) $f(t)$ is given by⁶⁰

$$\frac{\partial f(t)}{\partial t} + \dot{\mathbf{k}} \cdot \nabla_{\mathbf{k}} f(t) = -\frac{f(t) - \tilde{f}_{\text{eq}}}{\tau}, \quad (5)$$

where $\tilde{f}_{\text{eq}} = [1 + e^{\beta(\tilde{\epsilon}_{\mathbf{k}} - \mu)}]^{-1}$ is the Fermi-Dirac distribution function and τ is the relaxation time which is considered constant (energy independent) in our case. The NDF can be expressed as $f(t) = \tilde{f}_{\text{eq}} + \sum_{n=1}^{\infty} f_n(t)$, where the non-equilibrium part of the NDF can be understood as a power series of the electric field i.e., $f_n \propto E^n$. The recursive equation of f_n can be obtained from Eq. (5) to get the NDF up to quadratic order in an electric field.

A. Linear current responses

We begin with the study of current responses linear in E and up to linear order in B . To obtain the NDF linear in E , we consider the ansatz $f_1(t) = f_1^\omega e^{i\omega t} + f_1^{\omega*} e^{-i\omega t}$. Using the given ansatz in Eq. (5) and equating the terms corresponding to $e^{i\omega t}$ leads to

$$i\omega f_1^\omega - \frac{e}{\hbar D} [\mathbf{E} \cdot \nabla_{\mathbf{k}} \tilde{f}_{\text{eq}} + (\tilde{\mathbf{v}}_{\mathbf{k}} \times \mathbf{B}) \cdot \nabla_{\mathbf{k}} f_1^\omega] = -\frac{f_1^\omega}{\tau}. \quad (6)$$

By applying the Zener-Jones method approach⁶¹, we can express the linear order correction to the distribution function f_1^ω in terms of the infinite series of Lorentz force operator $\hat{\alpha}_B = (e/\hbar)[(\tilde{\mathbf{v}}_{\mathbf{k}} \times \mathbf{B}) \cdot \nabla_{\mathbf{k}}]$ as⁶²

$$f_1^\omega = \sum_{\eta=0}^{\infty} \left(\frac{\tau_\omega \hat{\alpha}_B}{D} \right)^\eta \left(\frac{e\tau_\omega}{\hbar D} \mathbf{E} \cdot \nabla_{\mathbf{k}} \tilde{f}_{\text{eq}} \right), \quad (7)$$

where $\tau_\omega = \tau/(1 + i\omega\tau)$. Taking into account the low strength of the B -field, the above equation can be expanded as a power series of the magnetic field⁵⁷. The equilibrium part of NDF \tilde{f}_{eq} consists of B -dependence through OMM-modified energy, thus it can be expanded via Taylor expansion in terms of B as $\tilde{f}_{\text{eq}} = f_{\text{eq}} - \epsilon_m f'_{\text{eq}}$, where $f'_{\text{eq}} \equiv \partial f_{\text{eq}} / \partial \epsilon_k$ with f_{eq} defined at $B = 0$.

The current responses linear in E can be expressed as $\mathbf{j}_1(t) = \mathbf{j}_{10}(t) + \mathbf{j}_{11}(t)$, where the first and second subscript represents the order of E and B respectively. The

magnetic field independent current of fundamental frequency can be expressed as $\mathbf{j}_{10}(t) = \mathbf{j}_{10}^\omega e^{i\omega t} + \mathbf{j}_{10}^{\omega*} e^{-i\omega t}$, where we obtain

$$\mathbf{j}_{10}^\omega = -\frac{e^2}{\hbar} \int [d\mathbf{k}] [\tau_\omega \mathbf{v}_\mathbf{k} (\mathbf{E} \cdot \nabla_\mathbf{k}) f_{\text{eq}} + (\mathbf{E} \times \boldsymbol{\Omega}) f_{\text{eq}}]. \quad (8)$$

The magnetic field independent conductivities take the following form

$$\sigma_{ab}^{(D)} = -e^2 \tau_\omega \int [d\mathbf{k}] v_a v_b f'_{\text{eq}}. \quad (9)$$

$$\sigma_{ab}^{(\text{AHC})} = -\frac{e^2}{\hbar} \varepsilon_{abd} \int [d\mathbf{k}] \Omega_d f_{\text{eq}}. \quad (10)$$

Equation (9) refers to the Drude conductivity, while Eq. (10) describes the intrinsic anomalous Hall conductivity which is independent of scattering time and vanishes for the TRS preserved system.

The magnetic field dependent current of fundamental frequency can be written as $\mathbf{j}_{11}(t) = \mathbf{j}_{11}^\omega e^{i\omega t} + \mathbf{j}_{11}^{\omega*} e^{-i\omega t}$, where we get

$$\mathbf{j}_{11}^\omega = \frac{e^2}{\hbar} \int [d\mathbf{k}] \left[(\mathbf{E} \times \boldsymbol{\Omega}) \epsilon_m f'_{\text{eq}} + \tau_\omega \mathbf{v}_\mathbf{k} \left\{ \frac{e}{\hbar} (\boldsymbol{\Omega} \cdot \mathbf{B}) (\mathbf{E} \cdot \nabla_\mathbf{k}) f_{\text{eq}} + (\mathbf{E} \cdot \nabla_\mathbf{k}) \epsilon_m f'_{\text{eq}} \right\} - \tau_\omega^2 \mathbf{v}_\mathbf{k} \hat{\alpha}_B (\mathbf{E} \cdot \nabla_\mathbf{k}) f_{\text{eq}} \right]. \quad (11)$$

The magnetic field-dependent conductivities which survive under TRS are given by

$$\sigma_{ab}^{(L)} = -\frac{e^3 \tau_\omega^2 B}{\hbar} \int [d\mathbf{k}] v_a (v_y \partial_{k_x} - v_x \partial_{k_y}) v_b f'_{\text{eq}}. \quad (12)$$

$$\sigma_{ab}^{(\text{OMM})} = \frac{e^2}{\hbar} \varepsilon_{abd} \int [d\mathbf{k}] \Omega_d \epsilon_m f'_{\text{eq}}. \quad (13)$$

The conductivity arising from current proportional to τ_ω in Eq. (11) vanishes since Ω_k , v_k and ϵ_m are odd under the TRS. Equation (12) represents the Lorentz force contribution (classical Hall effect), while Eq. (13) describes the OMM-induced Hall effect.

B. Second-order nonlinear current responses

Next, we move on to the study of nonlinear current responses quadratic in E and up to linear order in B .

The ansatz to calculate the NDF quadratic in E is given by

$$f_2(t) = f_2^0 + f_2^{0*} + f_2^{2\omega} e^{i2\omega t} + f_2^{2\omega*} e^{-i2\omega t}, \quad (14)$$

where f_2^0 denotes the rectification part and $f_2^{2\omega}$ denotes the second harmonic part of the NDF. Substituting it in Eq. (5) and equating the coefficients proportional to $e^{i2\omega t}$, we obtain

$$2i\omega f_2^{2\omega} - \frac{e}{\hbar D} [\mathbf{E} \cdot \nabla_\mathbf{k} f_1^\omega + (\tilde{\mathbf{v}}_\mathbf{k} \times \mathbf{B}) \cdot \nabla_\mathbf{k} f_2^{2\omega}] = -\frac{f_2^{2\omega}}{\tau}, \quad (15)$$

which gives⁶²

$$f_2^{2\omega} = \sum_{\eta=0}^{\infty} \left(\frac{\tau_{2\omega} \hat{\alpha}_B}{D} \right)^\eta \left(\frac{e\tau_{2\omega}}{\hbar D} \mathbf{E} \cdot \nabla_\mathbf{k} f_1^\omega \right), \quad (16)$$

where $\tau_{2\omega} = \tau/(1 + 2i\omega\tau)$ and $f_2^0 = f_2^{2\omega}(\mathbf{E} \rightarrow \mathbf{E}^*, \tau_{2\omega} \rightarrow \tau)$. The second harmonic NL current can be written as $\mathbf{j}_2(t) = \mathbf{j}_{20}(t) + \mathbf{j}_{21}(t)$. The magnetic field independent second harmonic current can be further expressed as $\mathbf{j}_{20}(t) = \mathbf{j}_{20}^\omega e^{2i\omega t} + \mathbf{j}_{20}^{\omega*} e^{-2i\omega t}$, where we obtain

$$\mathbf{j}_{20}^\omega = \frac{-e^3 \tau_\omega}{\hbar} \int [d\mathbf{k}] \left[(\mathbf{E} \times \boldsymbol{\Omega}) + \tau_{2\omega} \mathbf{v}_\mathbf{k} (\mathbf{E} \cdot \nabla_\mathbf{k}) \right] (\mathbf{E} \cdot \mathbf{v}_\mathbf{k}) f'_{\text{eq}}. \quad (17)$$

The corresponding NL conductivity is given by

$$\sigma_{abc}^{(\text{NAH})} = -\frac{e^3 \tau_\omega}{2\hbar} \varepsilon_{abd} \int [d\mathbf{k}] \Omega_d v_c f'_{\text{eq}} + (b \leftrightarrow c). \quad (18)$$

The above equation denotes the NL anomalous Hall conductivity which is proportional to the dipole moment of Berry curvature over occupied states, defined as $D_{bd} = -\int [d\mathbf{k}] (\nabla_{k_b} \epsilon_\mathbf{k}) \Omega_d f'_{\text{eq}}$. It is evident from the expression that Berry curvature dipole moment survives in time-reversal symmetric and inversion symmetry broken system, unlike the linear anomalous Hall conductivity. The second term in Eq. (17) corresponds to NL Drude conductivity (originating from band velocity) calculated as $\sigma_{abc}^{(D)} = -(e^3 \tau_\omega \tau_{2\omega} / \hbar) \int [d\mathbf{k}] v_a \partial_{k_b} v_c f'_{\text{eq}}$. The NL Drude conductivity vanishes if either of the symmetries between TRS and space inversion symmetry is present in contrast to linear Drude conductivity which is always nonzero.

The second harmonic NL current linearly dependent on the magnetic field can be written as $\mathbf{j}_{21}(t) = \mathbf{j}_{21}^{2\omega} e^{2i\omega t} + \mathbf{j}_{21}^{2\omega*} e^{-2i\omega t}$, where

$$\begin{aligned}
\mathbf{j}_{21}^{2\omega} = & \frac{e^3}{\hbar} \int [d\mathbf{k}] \left\{ (\mathbf{E} \times \boldsymbol{\Omega}) \left[\tau_{\omega} \left(\left(\frac{e}{\hbar} (\boldsymbol{\Omega} \cdot \mathbf{B}) \mathbf{v}_{\mathbf{k}} + \mathbf{v}_{\mathbf{k}}^m \right) f'_{\text{eq}} + \epsilon_m \mathbf{v}_{\mathbf{k}} f''_{\text{eq}} \right) \cdot \mathbf{E} - \tau_{\omega}^2 \hat{\alpha}_B (\mathbf{E} \cdot \mathbf{v}_{\mathbf{k}}) f'_{\text{eq}} \right] \right. \\
& + \tau_{\omega} \tau_{2\omega} \mathbf{v}_{\mathbf{k}} \mathbf{E} \cdot \left[\frac{e}{\hbar} (\boldsymbol{\Omega} \cdot \mathbf{B}) \nabla_{\mathbf{k}} (\mathbf{E} \cdot \mathbf{v}_{\mathbf{k}} f'_{\text{eq}}) + \nabla_{\mathbf{k}} \left(\frac{e}{\hbar} (\boldsymbol{\Omega} \cdot \mathbf{B}) (\mathbf{E} \cdot \mathbf{v}_{\mathbf{k}}) f'_{\text{eq}} + \mathbf{E} \cdot (\mathbf{v}_{\mathbf{k}}^m f'_{\text{eq}} + \epsilon_m \mathbf{v}_{\mathbf{k}} f''_{\text{eq}}) \right) \right] \\
& \left. - \tau_{\omega} \tau_{2\omega} \left[\mathbf{v}_{\mathbf{k}}^m \mathbf{E} \cdot \nabla_{\mathbf{k}} (\mathbf{E} \cdot \mathbf{v}_{\mathbf{k}} f'_{\text{eq}}) + \mathbf{v}_{\mathbf{k}} \left(\tau_{2\omega} \hat{\alpha}_B (\mathbf{E} \cdot \nabla_{\mathbf{k}} (\mathbf{E} \cdot \mathbf{v}_{\mathbf{k}} f'_{\text{eq}})) + \tau_{\omega} \mathbf{E} \cdot \nabla_{\mathbf{k}} (\hat{\alpha}_B (\mathbf{E} \cdot \mathbf{v}_{\mathbf{k}}) f'_{\text{eq}}) \right) \right] \right\} \quad (19)
\end{aligned}$$

In the above expression, terms proportional to τ and τ^3 vanish in the presence of TRS. Thus nonzero contribution for B -linear dependent NL current comes from the term $\propto \tau^2$. It is to be noted that in the presence of SIS but broken TRS, all these contributions vanish. Therefore breaking of SIS elicit these nonzero second-order NL responses. The corresponding NL conductivities are obtained as

$$\sigma_{abc}^{(\text{NAL})} = \frac{e^4 \tau_{\omega}^2 B}{2\hbar^2} \varepsilon_{abd} \int [d\mathbf{k}] \Omega_d (\mathbf{v} \times \nabla_{\mathbf{k}})_z (v_c f'_{\text{eq}}) + (b \leftrightarrow c). \quad (20)$$

The above equation describes the second-order NL Hall conductivity emerging from the combined effects of Lorentz force and anomalous velocity. The NL conductivity incited by OMM is given by

$$\begin{aligned}
\sigma_{abc}^{(\text{OMM})} = & \frac{e^3 \tau_{\omega} \tau_{2\omega}}{2\hbar} \int [d\mathbf{k}] [v_{ma} \partial_{k_b} (v_c f'_{\text{eq}}) \\
& + v_a \partial_{k_b} (v_{mc} f'_{\text{eq}} + \epsilon_m v_c f''_{\text{eq}})] + (b \leftrightarrow c). \quad (21)
\end{aligned}$$

Here, f''_{eq} is the double derivative of f_{eq} w.r.t energy. The contribution to the NL conductivity generated by the phase-space factor is obtained as

$$\begin{aligned}
\sigma_{abc}^{(\text{B})} = & \frac{e^4 \tau_{\omega} \tau_{2\omega}}{2\hbar^2} \int [d\mathbf{k}] [v_a ((\boldsymbol{\Omega} \cdot \mathbf{B}) \partial_{k_b} \\
& + \partial_{k_b} (\boldsymbol{\Omega} \cdot \mathbf{B})) v_c f'_{\text{eq}}] + (b \leftrightarrow c). \quad (22)
\end{aligned}$$

We emphasize that all the above three contributions to the second-order NL conductivities in the presence of a magnetic field depend on intrinsic band geometric quantities, namely Berry curvature and OMM. It is important to note that in experimental setups^{46,63}, the ac frequency lies in the range of 10 – 1000 Hz and relaxation time $\tau \sim 10^{-12}$ s, which explains the transport limit, i.e., $\omega_c \tau \ll 1$. Hence both the NL DC and second harmonic conductivities are equal such that $\sigma_{abc}^{(2\omega)}(\omega \rightarrow 0) = \sigma_{abc}^{\text{nl-dc}}$. In our work, we have assumed this transport limit to calculate the conductivities and resistivities of the system.

This section yields the general formalism for calculating the second-order NL current responses up to linear order in a magnetic field. In the upcoming sections, we will apply this formalism to the semi-Dirac model with the merging Dirac nodes for $\delta_0 \geq 0$ and investigate its linear and nonlinear transport properties in the presence of a low B -field. We will also discuss the contribution of band geometric quantities, i.e., Berry curvature and OMM to the linear and NL magnetoconductivities.

III. GAPPED SEMI-DIRAC SYSTEM

The low-energy Hamiltonian in \mathbf{k} -representation that describes the merging of two Dirac nodes has the following form^{18,22,55}

$$H(\mathbf{k}) = (\alpha k_x^2 - \delta_0) \sigma_x + v k_y \sigma_y + m_0 \sigma_z, \quad (23)$$

where $\boldsymbol{\sigma} = (\sigma_x, \sigma_y, \sigma_z)$ are the 2×2 Pauli matrices in pseudospin space, \mathbf{k} is the crystal momentum having magnitude, $k = \sqrt{k_x^2 + k_y^2}$, δ_0 and m_0 are the gap parameter, $\alpha = \hbar^2/2m^*$ with m^* as effective mass related to the x -direction and v is the Dirac velocity along the y -direction.

The energy spectrum is given by

$$\epsilon_{\lambda}(\mathbf{k}) = \lambda \sqrt{(\alpha k_x^2 - \delta_0)^2 + v^2 k_y^2 + m_0^2}, \quad (24)$$

where $\lambda = \pm$ denotes the conduction and valence band respectively. The corresponding band dispersion is shown in Fig. 1. The x -component of semiclassical band velocity is calculated as $\hbar v_x = 2\alpha k_x (\alpha k_x^2 - \delta_0)/\epsilon_{\mathbf{k}}$ and its y -component is $\hbar v_y = v^2 k_y/\epsilon_{\mathbf{k}}$.

Equation (23) has been termed the “Universal Hamiltonian” as different types of the spectrum can be obtained by tuning the gap parameter δ_0 ¹⁸. The Hamiltonian with $\delta_0 > 0$ describes the phase that consists of two Dirac nodes separated by $2\sqrt{\delta_0/\alpha}$ distance along the k_x axis. In the limit of $\delta_0 = 0$, the two Dirac nodes merge and the resulting dispersion reduces to semi-Dirac form. For $\delta_0 < 0$, a trivial insulating phase is obtained with a nonzero energy gap. Thus the variation of parameter δ_0 from negative to positive values drives the transition from an insulating phase to a semi-metallic phase. The mass term $m_0 \sigma_z$ is added in the Hamiltonian to introduce an energy gap at the Dirac nodes.

We employ the method of parameterization to the constant energy contours $\epsilon(\mathbf{k})$ in Eq. (24) considering the sign of k_x ($k_x \leq 0$) in each half-plane. The change of coordinates goes as²²

$$\alpha k_x^2 - \delta_0 = r \cos \phi, \quad v k_y = r \sin \phi, \quad \zeta_k = \text{sgn}(k_x) = \pm. \quad (25)$$

Here, the energy spectrum acquires the simplified form, $\epsilon_{\mathbf{k}} = \pm \sqrt{r^2 + m_0^2}$ and ϕ represents the coordinate along the constant energy contour. The limit of ϕ varies according to the topology of the constant energy contours

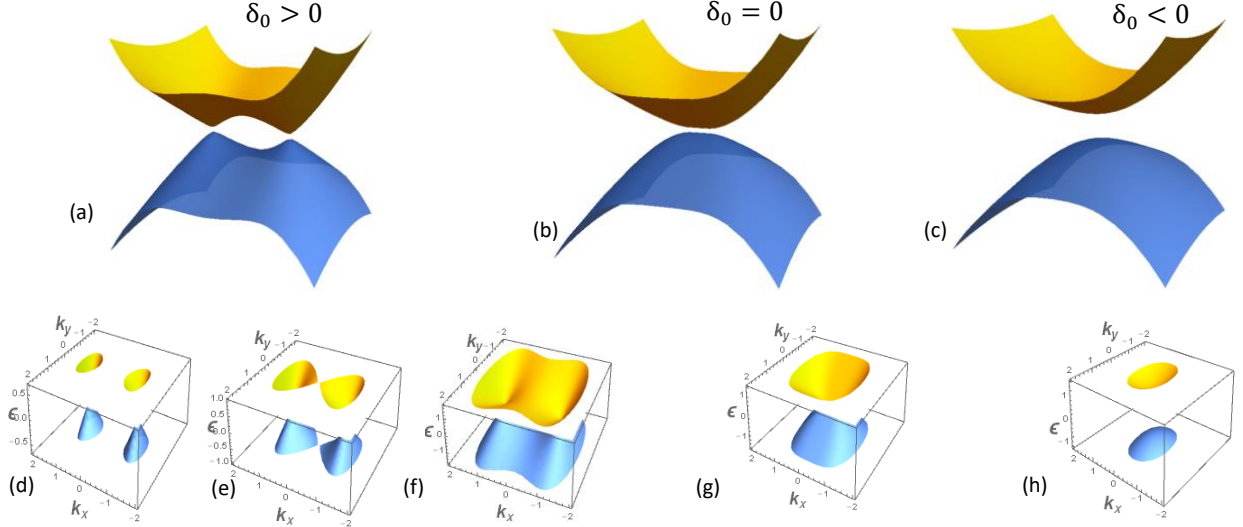


FIG. 1: Top panel (a)-(c) represents the energy spectrum of the model given by Eq. (23) for different values of gap parameter δ_0 . Plot (a) shows the case of $\delta_0 > 0$ describing the phase with two Dirac nodes separated by $2\sqrt{\delta_0/\alpha}$ distance along k_x direction, (b) $\delta_0 = 0$ corresponds to the semi-Dirac form where two Dirac nodes merge and (c) represents the gapped phase. Bottom panel (d)-(h) illustrates the constant Fermi energy contours corresponding to different values of δ_0 and Fermi energy. (d)-(f) describes the energy contours existing for three scenarios when $\delta_0 > 0$. (d) represent the two disconnected Fermi surfaces in accordance with the two distinct Dirac nodes till $\delta_0 > \sqrt{\mu^2 - m_0^2}$, (e) the two Fermi surfaces get connected by a saddle point at $\delta_0 = \sqrt{\mu^2 - m_0^2}$ and (f) the single connected Fermi surface exists as long as $\delta_0 < \sqrt{\mu^2 - m_0^2}$. (g) and (h) describes the constant Fermi energy contours for $\delta_0 = 0$ and $\delta_0 < 0$ respectively. Here, we have used $v = 65$ meV-nm, $m_0 = 0.1$ eV, $\alpha = 2.7$ meV-nm² with $m^* = 13.6 m_e$ for (TiO₂)₅/(VO₂)₃, where m_e is the electron mass.

obtained for different energies. The eigenstates are given by

$$\psi_{\mathbf{k}}^{\pm}(\mathbf{r}) = e^{i\mathbf{k}\cdot\mathbf{r}} \begin{pmatrix} \frac{\pm r}{\sqrt{r^2 + (\sqrt{r^2 + m_0^2} \mp m_0)^2}} \\ \frac{(\sqrt{r^2 + m_0^2} \mp m_0) e^{i\phi}}{\sqrt{r^2 + (\sqrt{r^2 + m_0^2} \mp m_0)^2}} \end{pmatrix}. \quad (26)$$

Next, we discuss the constant Fermi energy contours corresponding to different values of δ_0 and Fermi energy. For a given Fermi energy in the conduction band, the band contains only one minima at $\delta_0 = 0$. Hence, we get a single Fermi surface as a result of one nodal point (semi-Dirac node). When δ_0 starts to increase, the single minima splits into two minima giving rise to two allowed wave vectors that correspond to two distinct Dirac nodes with linear dispersion. A single connected Fermi surface continues to exist till $\delta_0 < \sqrt{\mu^2 - m_0^2}$ and the area of the Fermi surface gets enhanced due to the presence of extra curvature emerging from the splitting of single minima. These two Dirac points are connected by a saddle point which on a further increase of δ_0 yield two connected Fermi surfaces at $\delta_0 = \sqrt{\mu^2 - m_0^2}$. The two disconnected Fermi surfaces are formed for $\delta_0 > \sqrt{\mu^2 - m_0^2}$ which marks the onset of a decrease in the Fermi surface area since the bands get narrower with the increase of δ_0 . The Fermi surface topology nearly remains uninterrupted with δ_0 for high Fermi energy. Thus the range of

$\phi \in [-\phi_0, \phi_0]$ can be separated into two regions for the case of $\delta_0 > 0$,

$$\phi_0 = \begin{cases} \arccos \left[\frac{-\delta_0}{\sqrt{\mu^2 - m_0^2}} \right], & \delta_0 < \sqrt{\mu^2 - m_0^2}, \\ \pi, & \delta_0 \geq \sqrt{\mu^2 - m_0^2}. \end{cases} \quad (27)$$

The Jacobian for the transformation of coordinates from (k_x, k_y) to (r, ϕ) is given by

$$J(r, \phi) = \frac{r}{2v\sqrt{\alpha(r \cos \phi + \delta_0)}}. \quad (28)$$

We obtain the density of states (DOS) given as

$$D(\mu) = 2 \frac{1}{\pi^2 v \sqrt{8\alpha}} \sqrt{\frac{\delta_0^2 + m_0^2 \gamma^2}{\gamma \delta_0}} \begin{cases} K(k), & \gamma < 1, \\ k' [K(k')], & \gamma \geq 1, \end{cases} \quad (29)$$

where we introduce $\gamma = \delta_0 / \sqrt{\mu^2 - m_0^2}$ as a reduced parameter, $K(k)$ and $E(k)$ is the complete elliptic integral of a first and second kind respectively with $k = \sqrt{(1+\gamma)/2}$ and $k' = 1/k = \sqrt{2/(1+\gamma)}$ known as the modulus of Jacobian elliptic function and integrals. Note that an overall factor of 2 is multiplied to consider the sign of k_x . We choose $\mu > m_0$ such that the Fermi energy lies above the bulk gap. Expanding the above expression of DOS for $\gamma \geq 1$ up to leading order in k' gives

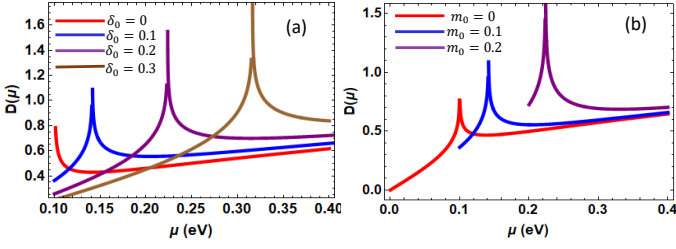


FIG. 2: Variation of the density of states (in units of 10^{-8} $\text{meV}^{-1}\text{-nm}^{-2}$) as a function of Fermi energy: (a) at fixed $m_0=0.1$ eV for different values of δ_0 and (b) at fixed $\delta_0=0.1$ eV for given values of m_0 . The parameters used are the same as in Fig. 1.

$$D(\mu) \simeq \frac{1}{32\pi v\sqrt{\alpha}} \sqrt{\frac{\delta_0^2 + m_0^2\gamma^2}{\gamma\delta_0}} \left(\frac{33 + 40\gamma + 16\gamma^2}{(1 + \gamma)^{5/2}} \right). \quad (30)$$

Near the band-edge in the limit of $\gamma \rightarrow \infty$, $D(\mu) \propto 1/\sqrt{\delta_0}$. For very low doping, DOS decreases with δ_0 whereas, for high doping, DOS increases with δ_0 and matches with semi-Dirac result in the large μ limit as shown in Fig. 2(a). Note that divergence occurs exactly at the saddle point ($\gamma = 1$). Equation 29 at $m_0 = 0$ reduces to the known results¹⁸. We also plotted the variation of DOS with Fermi energy at fixed $\delta_0 = 0.1$ eV for different values of energy gap parameter m_0 in Fig. 2(b). We find that as we increase the value of m_0 from 0.0 to 0.1, the peak of divergence also gets shifted since the allowed range of μ will also change from $\mu=0.0$ to 0.1 such that $\mu > m_0$ to get the physical results.

The Berry curvature and OMM of the given Hamiltonian can be calculated using Eqs. (3) and (4) as

$$\Omega_z = \mp \frac{\alpha v m_0 k_x}{\epsilon_{\mathbf{k}}^3}. \quad (31)$$

$$m_z = -\frac{e}{\hbar} \frac{\alpha v m_0 k_x}{\epsilon_{\mathbf{k}}^2}. \quad (32)$$

It is to be noted that Berry curvature and OMM are zero for the gapless system ($m_0 = 0$), whereas, in the limit of $\delta_0 = 0$, it remains nonzero. The OMM is the same for both the bands. The density-contour plot of the Berry curvature and OMM for the conduction band are shown in Fig. 3. The magnitude of Berry curvature decays rapidly as compared to OMM when Fermi energy shifts away from the band edge.

A. Linear conductivities

In this section, we calculate the linear conductivities of the gapped semi-Dirac Hamiltonian given by Eq. (23) in the presence of a static magnetic field applied along the z direction. We have explicitly used the general form of the Eqs. (9), (12)-(13) and modified coordinates which take into consideration the anisotropy of dispersion to

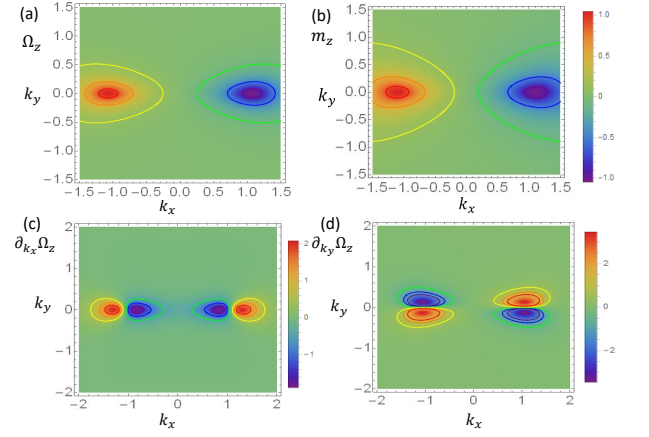


FIG. 3: Density-contour plot of (a) Berry curvature (in units of 10^{-1} nm^2), (b) OMM (in units of $4 \alpha e/\hbar$), (c) and (d) derivative of Berry curvature with respect to k_x and k_y respectively for the conduction band of the system. Here, k_x and k_y are plotted in units of $\sqrt{\delta_0/\alpha}$. The parameters used are the same as in Fig. 1.

evaluate the linear conductivities up to linear order in a magnetic field.

In the limit of zero temperature, a derivative of the Fermi-Dirac distribution function is substituted by the Dirac-delta function which allows performing the integral over energy analytically. Firstly, we start with the evaluation of linear conductivities in the absence of a magnetic field, i.e., the Drude conductivities along the x and y direction respectively. The Drude conductivity along the x direction after integration over energy takes the following form

$$\sigma_{xx}^{(D)} = \frac{e^2 \tau_\omega \sqrt{\alpha}}{v \pi^2 \hbar^2} \frac{\delta_0^{5/2}}{\sqrt{\gamma^3 (\delta_0^2 + m_0^2 \gamma^2)}} \int_{-\phi_0}^{\phi_0} d\phi \cos^2 \phi \sqrt{\cos \phi + \gamma}. \quad (33)$$

Next, we proceed with the angular integration by considering the appropriate limits of ϕ in accordance with the three regimes discussed in Eq. (27) for $\delta_0 > 0$. Such integrals can be expressed in terms of complete elliptic integrals of the first and second kinds. The xx -component of Drude conductivity is given by

$$\sigma_{xx}^{(D)} = \frac{2\sqrt{2}e^2 \tau_\omega \sqrt{\alpha}}{15v\pi^2 \hbar^2} \frac{\delta_0^{5/2}}{\sqrt{\gamma^3 (\delta_0^2 + m_0^2 \gamma^2)}} \begin{cases} [(2\gamma^2 + 7\gamma - 9)K(k) + 2(9 - 2\gamma^2)E(k)], & \gamma < 1, \\ 2k[(9 - 2\gamma^2)E(k') + 2\gamma(\gamma - 1)K(k')], & \gamma \geq 1, \end{cases} \quad (34)$$

In view of anisotropic dispersion, $\sigma_{xx}^{(D)} \neq \sigma_{yy}^{(D)}$. Following the details of calculation similar to xx -term, the yy -

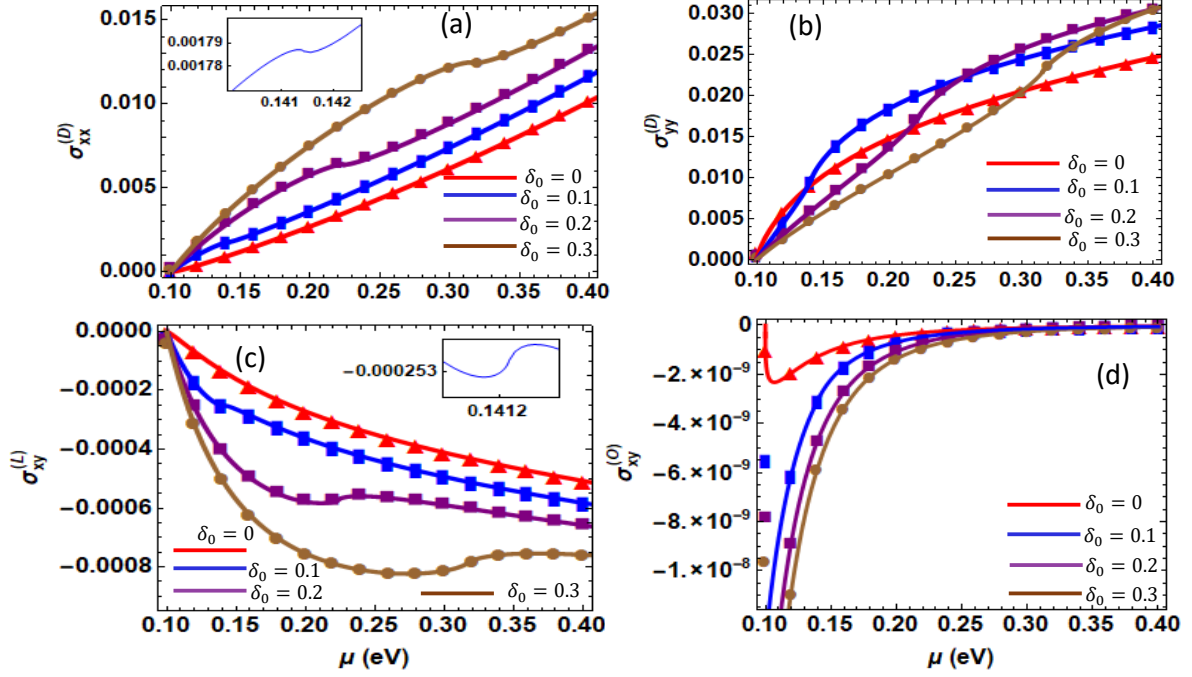


FIG. 4: Variation of linear conductivities (up to linear order in B) with the Fermi energy for different values of δ_0 . (a)-(b) Drude conductivity along the x and y direction respectively, (c) Lorentz force induced linear Hall conductivity, and (d) Orbital magnetic moment induced linear Hall conductivity. Here, the solid color curves represent the results of analytical calculations at zero temperature whereas the corresponding colored plot markers are the representatives of the results of numerical calculations performed at temperature $T = 34$ K. The inset is a blow-up of the region around $\mu = \sqrt{\delta_0^2 + m_0^2}$ for $\delta_0 = 0.1$ eV. The above linear conductivities are plotted in units of A/V. The parameters used are $v = 65$ meV-nm, $\alpha = 2.7$ meV-nm² with $m^* = 13.6m_e$, $\tau = 10^{-12}$ s, $B = 2$ T and $m_0 = 0.1$ eV.

component of Drude conductivity is calculated to be

$$\sigma_{yy}^{(D)} = \frac{\sqrt{2}e^2\tau\omega v}{3\pi^2\hbar^2\sqrt{\alpha}} \frac{\delta_0^{3/2}}{\sqrt{\gamma(\delta_0^2 + m_0^2\gamma^2)}} \begin{cases} [2\gamma E(k) + (1-\gamma)K(k)], & \gamma < 1, \\ 2k[\gamma E(k') - (\gamma-1)K(k')], & \gamma \geq 1. \end{cases} \quad (35)$$

We have plotted the Drude conductivities $\sigma_{xx}^{(D)}$ and $\sigma_{yy}^{(D)}$

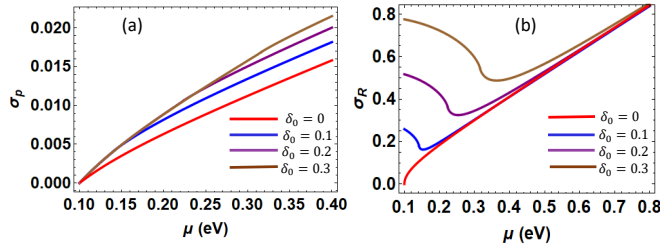


FIG. 5: (a)-(b) Plots of variation of $\sigma_P \equiv \sqrt{\sigma_{xx}^{(D)} \sigma_{yy}^{(D)}}$ and $\sigma_R \equiv \sigma_{xx}^{(D)} / \sigma_{yy}^{(D)}$ with the Fermi energy for different values of δ_0 . The solid color curves represent the analytical results calculated at zero temperature. All parameters used are the same as in Fig. 4.

as a function of Fermi energy at the given values of δ_0

in Figs. 4(a) and 4(b). The behavior of conductivities is expectedly different for $\gamma < 1$ (high Fermi energy with single-connected Fermi surface) and $\gamma \geq 1$ (low Fermi energy with two Fermi surfaces) due to the particular Fermi surface topology in the two regimes. For the case of $\gamma \geq 1$, expanding the exact analytic expressions given by Eqs. (34) and (35) up to leading order in k' , we get

$$\sigma_{xx}^{(D)} \simeq \frac{e^2\tau\omega\sqrt{\alpha}}{8v\pi\hbar^2} \frac{\delta_0^{5/2}}{\sqrt{\gamma^3(\delta_0^2 + m_0^2\gamma^2)}} \left[\frac{(1+2\gamma)(3+4\gamma)}{(\gamma+1)^{3/2}} \right], \quad (36)$$

$$\sigma_{yy}^{(D)} \simeq \frac{e^2\tau\omega v}{16\pi\hbar^2\sqrt{\alpha}} \frac{\delta_0^{3/2}}{\sqrt{\gamma(\delta_0^2 + m_0^2\gamma^2)}} \left[\frac{(11+4\gamma)}{(\gamma+1)^{3/2}} \right]. \quad (37)$$

In the limit of $\gamma \rightarrow \infty$ (near the band edge approximation i.e., $\mu \rightarrow m_0$), we find that $\sigma_{xx}^{(D)} \propto \mu^2\sqrt{\delta_0}$ and $\sigma_{yy}^{(D)} \propto \mu^2/\sqrt{\delta_0}$. Hence, for low doping, $\sigma_{xx}^{(D)}$ increases with both μ and δ_0 , whereas $\sigma_{yy}^{(D)}$ increases with the Fermi energy but decreases with δ_0 . We noticed a small kink in both the Drude conductivities as a consequence of a change in Fermi surface topology exactly at the saddle point ($\gamma = 1$) for the fixed positive values of δ_0 . For high doping, $\sigma_{xx}^{(D)}$ and $\sigma_{yy}^{(D)}$ continues to increase with

the Fermi energy. The increasing nature of Drude conductivities with the Fermi energy can be explained by the monotonous increase of Fermi surface area and velocities with μ for given δ_0 . It is to be noted that for high Fermi energy, the Fermi surface topology relatively remains the same with δ_0 .

We also note the variation for the geometric mean of Drude conductivities defined as $\sigma_P = \sqrt{\sigma_{xx}^{(D)} \sigma_{yy}^{(D)}}$ and their ratio $\sigma_R \equiv \sigma_{xx}^{(D)} / \sigma_{yy}^{(D)}$ with μ and δ_0 . We are interested in probing the variations of experimentally relevant quantity σ_R which is independent of scattering time since the calculation of scattering time may not be straightforward. Similar to Drude conductivities, σ_P also shows an increase with the Fermi energy. However, the ratio σ_R decreases with Fermi energy for low doping while for high doping, it shows an increase with the Fermi energy for a given δ_0 . Note that for low doping, the semi-Dirac curve ($\delta_0 = 0$) for σ_R deviates significantly from the finite δ_0 case. For $\delta_0 = 0$, σ_R increases with the Fermi energy whereas decreases for finite δ_0 . For high doping, the resulting ratio curve matches perfectly well with the semi-Dirac case. Next, we discuss the variation of these quantities as a function of δ_0 for a given Fermi energy. We find that for low doping, σ_P is nearly constant which is consistent with our results of $\gamma \rightarrow \infty$ limit, while for high doping, σ_P shows an increase with δ_0 . The ratio σ_R increases with δ_0 . This variation for the geometric mean and ratio of Drude conductivities are illustrated in Figs. 5(a) and 5(b) respectively.

Now we move to compute the magnetic field-dependent linear conductivities of the system. The Lorentz force-induced Hall conductivity can be calculated using Eq. (12) as

$$\sigma_{xy}^{(L)} = -\frac{2\sqrt{2}e^3\tau_\omega^2v\sqrt{\alpha}B}{15\pi^2\hbar^4} \frac{\delta_0^{5/2}}{\sqrt{\gamma}(\delta_0^2 + m_0^2\gamma^2)} \begin{cases} [(2\gamma^2 + 7\gamma - 9)K(k) + 2(9 - 2\gamma^2)E(k)], & \gamma < 1, \\ 2k[(9 - 2\gamma^2)E(k') + 2\gamma(\gamma - 1)K(k')], & \gamma \geq 1. \end{cases} \quad (38)$$

Here, $\sigma_{xy}^{(L)} = -\sigma_{yx}^{(L)}$. Expanding the low-energy expression up to the leading order in k' , we find

$$\sigma_{xy}^{(L)} \simeq \frac{-e^3\tau_\omega^2v\sqrt{\alpha}B}{8\pi\hbar^4} \frac{\delta_0^{5/2}}{\sqrt{\gamma}(\delta_0^2 + m_0^2\gamma^2)} \left[\frac{(1 + 2\gamma)(3 + 4\gamma)}{(\gamma + 1)^{3/2}} \right]. \quad (39)$$

In the limit of $\gamma \rightarrow \infty$, it turns out that $\sigma_{xy}^{(L)} \propto (\mu^2)\sqrt{\delta_0}$. The variation of $\sigma_{xy}^{(L)}$ with the Fermi energy is shown in Fig. 4(c). Below the saddle point for $\gamma > 1$, $\sigma_{xy}^{(L)}$ increases with the increase in Fermi energy and δ_0 . In other words, $\sigma_{xy}^{(L)}$ decreases as Dirac nodes moves closer to each other ($\delta_0 \rightarrow 0$). As expected, a little kink is observed at the saddle point. Past the saddle point, $\sigma_{xy}^{(L)}$ continues to monotonically increasing with μ . For high Fermi energy, $\sigma_{xy}^{(L)}$ increases with δ_0 .

The OMM-induced Hall conductivity can be evaluated

using Eq. (13) as

$$\sigma_{xy}^{(\text{OMM})} = -\sigma_{yx}^{(\text{OMM})} = -\frac{e^3vm_0^2\sqrt{\alpha}B}{\sqrt{2\pi^2\hbar^2}} \frac{\sqrt{\gamma^7\delta_0}}{(\delta_0^2 + m_0^2\gamma^2)^2} \begin{cases} [2E(k) - (1 - \gamma)K(k)], & \gamma < 1, \\ 2k[E(k')], & \gamma \geq 1. \end{cases} \quad (40)$$

Expanding the above expression for $\gamma \geq 1$, we find

$$\sigma_{xy}^{(\text{OMM})} \simeq \frac{-e^3vm_0^2\sqrt{\alpha}B}{32\pi\hbar^2} \frac{\sqrt{\gamma^7\delta_0}}{(\delta_0^2 + m_0^2\gamma^2)^2} \left[\frac{(1 + 4\gamma)(5 + 4\gamma)}{(\gamma + 1)^{3/2}} \right]. \quad (41)$$

We find that the $\sigma_{xy}^{(\text{OMM})}$ varies as $\sqrt{\delta_0}$ in $\gamma \rightarrow \infty$ limit. For low doping, $\sigma_{xy}^{(\text{OMM})}$ decreases with the Fermi energy whereas increases with δ_0 . Above the saddle point, it continues to decrease with μ while increases with δ_0 . Note that this energy dependence of $\sigma_{xy}^{(\text{OMM})}$ is related to the fact that the magnitude of Berry curvature and OMM decreases as the Fermi energy shifts away from the band edge. It is evident from Fig. 4(d) that the magnitude of OMM induced Hall conductivity is considerably smaller than the other linear contributions.

We would like to point out that the linear conductivities $\sigma_{xx}^{(D)}$, $\sigma_{xy}^{(L)}$ and $\sigma_{xy}^{(\text{OMM})}$ are predicted to be large for materials with small effective mass, whereas $\sigma_{yy}^{(D)}$ appears small for low effective mass. The effective mass of some proposed semi-Dirac materials are $m^* = 13.6m_e$ for $(\text{TiO}_2)_5/(\text{VO}_2)_3$, $m^* = 3.1m_e$ (α -(BEDT-TTF) $_2\text{I}_3$) and $m^* = 1.2 \times 10^{-3}m_e$ (photonic crystals)⁵⁵. We have used $m^* = 13.6m_e$, $v = 65$ meV-nm, $m_0 = 0.1$ eV, $\alpha = 2.7$ meV-nm², $B = 2$ T and $\tau = 10^{-12}$ s in this work. We also find that the linear conductivities decrease with the increase of gap parameter m_0 at a given value of μ and δ_0 . It is to be noted that only the Hall components of the above B -linear contribution to the conductivity survive due to the Onsager relation which implies $\sigma_{ij}(B) = \sigma_{ji}(-B)$. We have also calculated these contributions to the linear conductivities numerically at $T = 34$ K and the obtained results at $T = 34$ K match well with the analytical results evaluated at zero temperature.

B. Nonlinear conductivities

Next, we calculate the different contributions (arising from Berry curvature and OMM) to the NL conductivities of the system. Following the details of calculation similar to the linear case related to the integration over energy and ϕ in two regimes, the NL anomalous Hall conductivity can be evaluated using Eq. (18) as

$$\sigma_{xyx}^{(\text{NAH})} = \frac{-e^3\tau_\omega m_0\sqrt{\alpha}}{3\sqrt{2\pi^2\hbar^2}} \frac{(\gamma\delta_0)^{3/2}}{(\delta_0^2 + m_0^2\gamma^2)^{3/2}} \begin{cases} [(1 - \gamma)K(k) + 2\gamma E(k)], & \gamma < 1, \\ 2k[(1 - \gamma)K(k') + \gamma E(k')], & \gamma \geq 1. \end{cases} \quad (42)$$

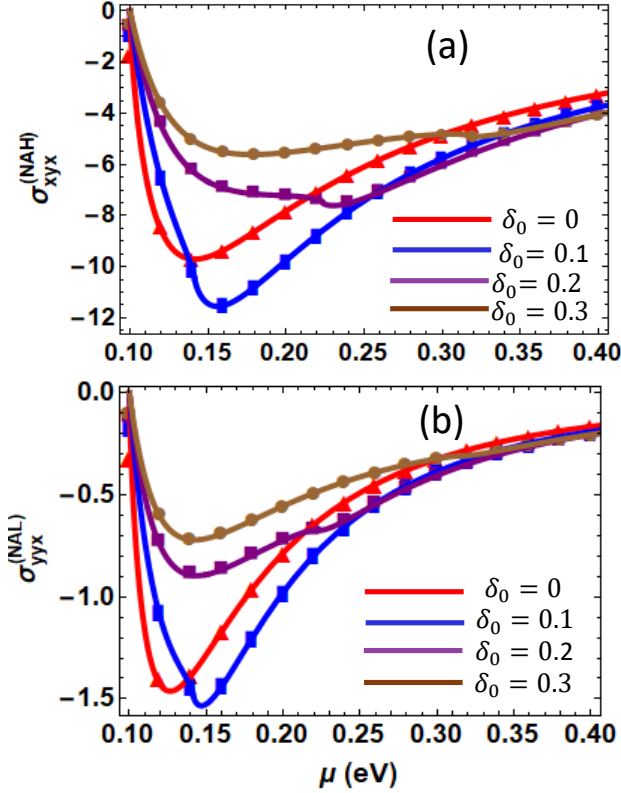


FIG. 6: (a) Depicts the behavior of nonlinear anomalous Hall conductivity with the Fermi energy. (b) The anomalous velocity and Lorentz force induced NL conductivity as a function of Fermi energy. Both of these plots are plotted for different values of δ_0 . The solid color curves are the results of analytical calculations at zero temperature which matches perfectly well with the numerical results obtained at $T = 34$ K (color plot markers). The above nonlinear conductivities are plotted in units of 10^{-4} nA.m/V². The parameters used are the same as in Fig. 4.

The other nonvanishing components of NL anomalous conductivity goes as $\sigma_{xxy}^{(NAH)} = \sigma_{xyx}^{(NAH)}$ and $\sigma_{yyx}^{(NAH)} = -2\sigma_{xyx}^{(NAH)}$. These off-diagonal terms are proportional to the x -component of the Berry curvature dipole which is nonzero due to the mirror symmetry along the x axis⁵⁵.

We obtained the NL Hall conductivity arising due to the effective combination of Lorentz force and anomalous velocity for the system using Eq. (20) and find it is related to NL anomalous Hall conductivity as

$$\sigma_{yyx}^{(NAL)} = \frac{ev^2\tau_\omega B}{\hbar^2\mu}\sigma_{xyx}^{(NAH)}. \quad (43)$$

The other nonzero Hall components are $\sigma_{xyy}^{(NAL)} = \sigma_{yyx}^{(NAL)}$ and $\sigma_{xxy}^{(NAL)} = -2\sigma_{yyx}^{(NAL)}$. It is evident from the above equation that the ratio $\sigma_{yyx}^{(NAL)}/\sigma_{xyx}^{(NAH)}$ is independent of δ_0 . Expanding the exact analytical results given by Eqs.

(42) and (43) for $\gamma \geq 1$, we obtain

$$\sigma_{xyx}^{(NAH)} \simeq \frac{-e^3\tau_\omega m_0\sqrt{\alpha}}{32\pi\hbar^2} \frac{(\gamma\delta_0)^{3/2}}{(\delta_0^2 + m_0^2\gamma^2)^{3/2}} \left[\frac{4\gamma + 11}{(1 + \gamma)^{3/2}} \right]. \quad (44)$$

$$\sigma_{yyx}^{(NAL)} \simeq \frac{ev^2\tau_\omega B}{\hbar^2} \frac{\gamma}{\sqrt{\delta_0^2 + m_0^2\gamma^2}} \sigma_{xyx}^{(NAH)}. \quad (45)$$

Near the band-edge at $\gamma \rightarrow \infty$, we find that $\sigma_{xyx}^{(NAH)}$ and $\sigma_{yyx}^{(NAL)} \propto \mu^2/\sqrt{\delta_0}$. For low doping, both the NL conductivities increase with μ but decrease with δ_0 . As Fermi energy is further increased, both $\sigma_{xyx}^{(NAH)}$ and $\sigma_{yyx}^{(NAL)}$ start decreasing with μ , although a substantial change is not observed with δ_0 in the region of high Fermi energy. A small kink is observed at the saddle point which reflects the change in Fermi surface topology. The Fermi energy dependence of $\sigma_{xyx}^{(NAH)}$ and $\sigma_{yyx}^{(NAL)}$ for different values of δ_0 is depicted in Figs. 6(a) and 6(b) respectively. The peaks in $\sigma_{yyx}^{(NAL)}$ appear to be more pronounced than the peaks seen in $\sigma_{xyx}^{(NAH)}$.

The phase-space contribution to the NL conductivity can be calculated using Eq. (22). Its expression after integration over energy (at zero temperature) is cumbersome and therefore not presented over here. The nonzero components of phase-space induced conductivity includes diagonal term $\sigma_{xxx}^{(B)}$ and off-diagonal components $\sigma_{yyx}^{(B)} = \sigma_{xyy}^{(B)}$ and $\sigma_{xxy}^{(B)}$. We have plotted the Fermi energy dependence of these terms for different values of δ_0 in Fig. 7. Similar to the linear case, we have plotted the above three contributions to the NL conductivity by performing numerical calculations at temperature $T = 34$ K and we observed that they agree closely with our analytical results obtained at zero temperature.

We next turn to evaluate the OMM contribution to the NL conductivity using Eq. (21). We start by performing the integral over energy analytically using the approximation $f'_{eq} = -\delta(\epsilon_{\mathbf{k}} - \mu)$ in the limit of $T \rightarrow 0$, where we find that the resulting expression encounters divergence, unlike the previous cases. Thus the zero temperature approximation of the Dirac-delta function does not capture the proper results here. Therefore we proceed to calculate the OMM contribution by computing the results numerically at finite temperature $T = 34$ K to overcome the issue of divergence. Figure 8 represents the variation of OMM induced NL conductivity ($\sigma_{yyx}^{(0MM)} = \sigma_{xyy}^{(0MM)} = \sigma_{yyx}^{(0MM)}$ and $\sigma_{xxy}^{(0MM)}$) with the Fermi energy. Both the NL conductivities, $\sigma_{abc}^{(0MM)}$ and $\sigma_{abc}^{(B)}$ initially show an increase with the Fermi energy but then start decreasing. In contrast to the other NL contributions, the OMM induced and a diagonal component of phase-space factor induced NL conductivity changes sign on variation with μ .

It is important to note that all the above NL conductivities have a peak near the band edge which is related to

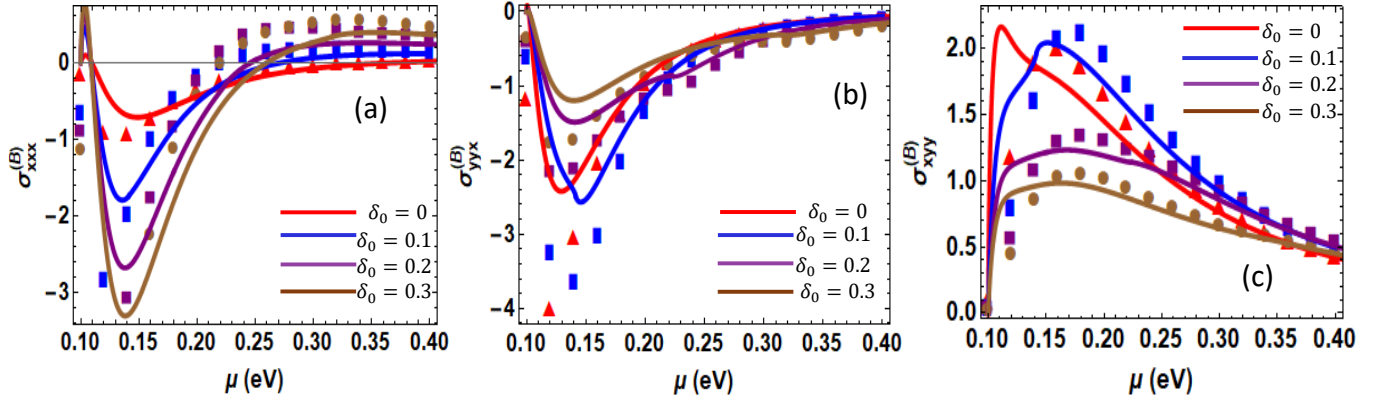


FIG. 7: (a)-(c) Variation of different components of phase-space factor induced nonlinear conductivity (in units of 10^{-4} nA.m/V²) with the Fermi energy for different values of δ_0 . The solid color curves are the results calculated at zero temperature, while color plot markers represent the numerical results obtained at $T = 34$ K. The parameters used are the same as in Fig. 4.

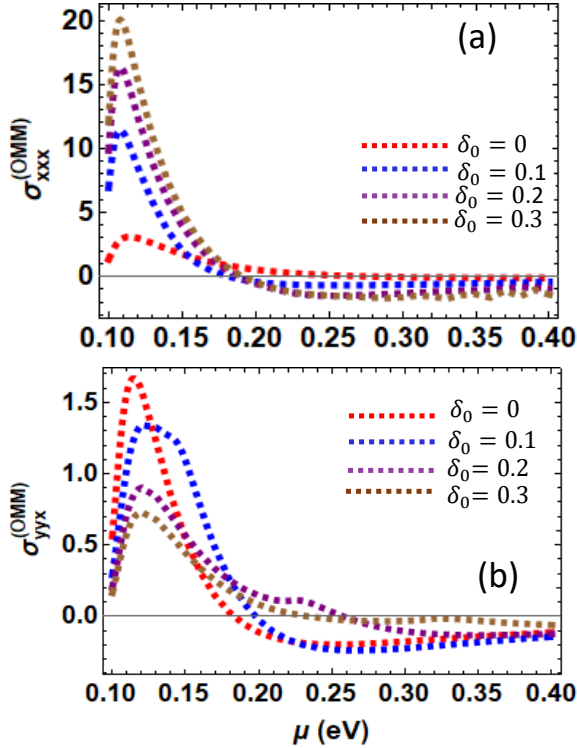


FIG. 8: (a)-(b) Orbital magnetic moment induced nonlinear conductivity as a function of Fermi energy for different values of δ_0 . The dashed color curves denote the results calculated numerically at $T = 34$ K. The above conductivities are plotted in units of 10^{-4} nA.m/V². The parameters used are the same as in Fig. 4.

the fact that these NL contributions arise from the Berry curvature and OMM and their magnitude decreases as the Fermi energy shifts from the band edge. The peaks are not observed exactly at the band edge because the NL contributions arise from the effective contribution of geometric quantities and band dispersion anisotropy. It

is worth pointing out that all four contributions to the NL conductivities increase with the decrease in the effective band mass of semi-Dirac materials. Interestingly, these NL conductivities in a given semi-Dirac material are found to be comparable or order smaller than the NL conductivities of a 2D system hosting massive tilted Dirac fermions⁶⁴. We also noticed the variation of NL conductivities with the gap parameter m_0 and find that their peak is shifted with the increase of m_0 .

IV. RESISTIVITY

We have calculated the linear and NL magnetoconductivities in the above section, we next calculate the experimentally measured linear and NL resistivities for the gapped semi-Dirac system. In response to an ac current j^ω flowing through the material in the experimental setups of NL transport^{46,64–66}, the induced linear electric field E^ω , the induced NL DC electric field $E^{\text{nl-dc}}$ and the induced NL second harmonic electric field $E^{2\omega}$ are measured. These induced electric fields are related to the applied current j^ω by introducing resistivity into the picture. The linear resistivity ρ_{ab} is defined as $E_a^\omega = \rho_{ab} j_b^\omega$, whereas NL DC resistivity goes as $E_a^{\text{nl-dc}} = \rho_{abc}^{\text{nl-dc}} j_b^\omega j_c^\omega$ and the second harmonic resistivity is given by $E_a^{2\omega} = \rho_{abc}^{(2\omega)} j_b^\omega j_c^\omega$.

A. Linear resistivity

The linear resistivity matrix can be simply obtained by inverting the linear conductivity matrix. Keeping the lowest order magnetic field dependence, the linear resistivities can be calculated using $\rho_{xx} = 1/\sigma_{xx}^{(D)}$, $\rho_{xy} = -\rho_{yx} = -\sigma_{xy}^{(L)}/(\sigma_{xx}^{(D)}\sigma_{yy}^{(D)})$ and $\rho_{yy} = 1/\sigma_{yy}^{(D)}$. Note that we have ignored the OMM induced Hall conductivity contribution as its magnitude is much small as compared to

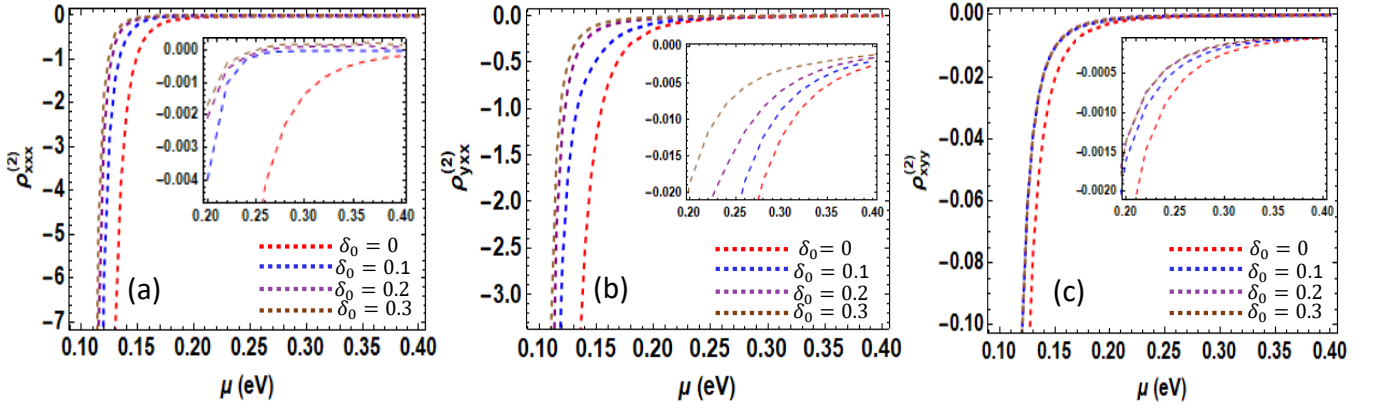


FIG. 9: (a) NL resistivity $\rho_{xxx}^{(2)}$ and (b) NL Hall resistivity $\rho_{yxx}^{(2)}$ as a function of Fermi energy for different values of δ_0 (when current is applied along the x -direction). (c) The variation of NL Hall resistivity $\rho_{xyy}^{(2)}$ with the Fermi energy (when current is applied along the y -direction). The insets represent the blow-up of the region where Fermi energy ranges from 0.2 eV to 0.4 eV. The dashed color curves represent the numerical results obtained at $T = 34$ K. The above nonlinear resistivities are plotted in units of 10^{-4} V m/A². The parameters used are the same as in Fig. 4.

Lorentz force induced Hall conductivity, $\sigma_{xy}^{(\text{OMM})} \ll \sigma_{xy}^{(\text{L})}$. We find that the linear longitudinal resistivity, $\rho_{xx} \propto B^0$ and linear Hall resistivity, $\rho_{xy} \propto B$. These linear resistivities show a decrease with Fermi energy.

B. Nonlinear resistivity

Unlike the linear resistivity case, the NL resistivity matrix cannot be obtained directly by inverting the NL conductivity matrix. Instead, the second-order NL resistivity is defined in terms of second-order NL conductivities and linear resistivities⁶⁴ as

$$\rho_{abc}^{(2)} = -\rho_{ai}\sigma_{ijk}\rho_{jb}\rho_{kc}. \quad (46)$$

Case I. Current applied along the x -direction: We consider that the current is flowing only along the x -direction, then the components of the NL resistivity matrix for 2D systems can be written as

$$\begin{pmatrix} \rho_{xxx}^{(2)} \\ \rho_{yxx}^{(2)} \end{pmatrix} = -[\rho] \begin{pmatrix} \sigma_{xxx} & \sigma_{xxy} & \sigma_{xyx} & \sigma_{xyy} \\ \sigma_{yxx} & \sigma_{yyx} & \sigma_{yyx} & \sigma_{yyy} \end{pmatrix} \begin{pmatrix} \rho_{xx}^2 \\ \rho_{xx}\rho_{yx} \\ \rho_{xx}\rho_{yx} \\ \rho_{yx}^2 \end{pmatrix}. \quad (47)$$

Here, $\rho_{xxx}^{(2)}$ and $\rho_{yxx}^{(2)}$ denote the NL longitudinal and NL Hall resistivities respectively and $[\rho]$ is the 2×2 linear resistivity matrix. We further simplify the above equation by keeping the lowest-order magnetic field dependence and ignoring the quadratic and higher B -field dependent terms lead to

$$\rho_{xxx}^{(2)} = -\rho_{xx}^2 (\sigma_{xxx}\rho_{xx} + 2\sigma_{xyx}\rho_{yx} + \sigma_{yxx}\rho_{xy}). \quad (48)$$

$$\rho_{yxx}^{(2)} = -\rho_{xx}^2 \sigma_{yxx}\rho_{yx}. \quad (49)$$

We find that the lowest-order magnetic field dependence of these second-order NL resistivities goes as $\rho_{xxx}^{(2)} \propto B$ and $\rho_{yxx}^{(2)} \propto B^0$ which is distinct from the linear resistivity. It is evident from Eq. (48) that $\rho_{xxx}^{(2)}$ depend on NL conductivities and linear Hall resistivities. Note that longitudinal resistivity ρ_{xxx} in the absence of magnetic field becomes zero as $\sigma_{xxx}(B=0) = 0$. Thus we emphasize that the predicted B -linear dependence of $\rho_{xxx}^{(2)}$ arises mainly from the diagonal component of NL conductivity ($\sigma_{xxx} = \sigma_{xxx}^{(\text{OMM})} + \sigma_{xxx}^{(\text{B})}$) which remains finite due to the surviving mirror symmetry along the x -direction. The NL resistivities originate from Berry curvature and OMM and therefore has a quantum mechanical origin. The NL resistivities $\rho_{xxx}^{(2)}$ and $\rho_{yxx}^{(2)}$ show a relatively significant decrease with the Fermi energy for low doping as compared to high doping which is illustrated in Figs. 9(a) and 9(b). Furthermore, the scattering time dependence of NL resistivities is found to be $\rho_{xxx}^{(2)} \propto 1/\tau$ and $\rho_{yxx}^{(2)} \propto 1/\tau^2$. Thus, the experimentally connected scattering time independent ratios are defined for NL resistivities as $\rho_{xxx}^{(2)}/\rho_{xx}$ and $\rho_{yxx}^{(2)}/\rho_{xx}^2$. We find that $\rho_{xxx}^{(2)}/\rho_{xx}$ (\sim ratio of NL longitudinal voltage to the product of linear voltage and current) decreases with the Fermi energy and δ_0 whereas $\rho_{yxx}^{(2)}/\rho_{xx}^2$ (\sim ratio of NL Hall voltage to the square of linear voltage) decreases with Fermi energy but independent of δ_0 . Unlike the linear and NL conductivities, the change in Fermi surface topology is not reflected in the NL resistivities through the kink.

Case II. Current applied along the y -direction: In the wake of anisotropic energy dispersion, the current is also applied along the y -direction and the corresponding NL

$j \propto E^n$	$B = 0$		$B \neq 0$		
	Drude	Anomalous Hall	Lorentz force and anomalous velocity (L)	phase-space factor (B)	Orbital Magnetic moment(OMM)
$n = 1$ linear current responses	$\sigma_{xx}^{(D)} \neq \sigma_{yy}^{(D)}$	0	$\sigma_{xy}^{(L)} = -\sigma_{yx}^{(L)}$	0	$\sigma_{xy}^{(OMM)} = -\sigma_{yx}^{(OMM)}$
$n = 2$ Nonlinear current responses	0	$\sigma_{xyx}^{(NAH)} = \sigma_{xxy}^{(NAH)}$ $\sigma_{yxx}^{(NAH)} = -2\sigma_{xyx}^{(NAH)}$	$\sigma_{yxy}^{(NAL)} = \sigma_{yyx}^{(NAL)}$ $\sigma_{xyy}^{(NAL)} = -2\sigma_{yxy}^{(NAL)}$	$\sigma_{xxx}^{(B)}, \sigma_{xyy}^{(B)}$ $\sigma_{yyx}^{(B)} = \sigma_{yxy}^{(B)}$	$\sigma_{xxx}^{(OMM)}, \sigma_{yxy}^{(OMM)} =$ $\sigma_{xyy}^{(OMM)} = \sigma_{yyx}^{(OMM)}$

TABLE I: Highlighting the nonzero components of different contributions induced by the Berry curvature and the OMM to the linear and second-order nonlinear conductivities (up to linear order in a magnetic field).

resistivity matrix turns out to be

$$\begin{pmatrix} \rho_{xyy}^{(2)} \\ \rho_{yyy}^{(2)} \end{pmatrix} = -[\rho] \begin{pmatrix} \sigma_{xxx} & \sigma_{xxy} & \sigma_{xyx} & \sigma_{xyy} \\ \sigma_{yxx} & \sigma_{yyx} & \sigma_{yxy} & \sigma_{yyy} \end{pmatrix} \begin{pmatrix} \rho_{xy}^2 \\ \rho_{xy}\rho_{yy} \\ \rho_{xy}\rho_{yy} \\ \rho_{yy}^2 \end{pmatrix}. \quad (50)$$

Focusing on the lowest-order magnetic field dependence terms, we get

$$\rho_{yyy}^{(2)} = 0, \quad (51)$$

$$\rho_{xyy}^{(2)} = -\rho_{xx}\rho_{yy}(2\sigma_{xyx}\rho_{xy} + \sigma_{xyy}\rho_{yy}). \quad (52)$$

Here, the NL longitudinal resistivity $\rho_{yyy}^{(2)}$ vanishes and the NL Hall resistivity $\rho_{xyy}^{(2)} \propto B$. The NL Hall resistivity $\rho_{xyy}^{(2)}$ in the absence of magnetic field comes zero as $\sigma_{xyy}(B=0) = 0$. Hence this B -linear dependence of $\rho_{xyy}^{(2)}$ originally arises from the NL Hall conductivity ($\sigma_{xyy} = \sigma_{xyy}^{(NAL)} + \sigma_{xyy}^{(OMM)} + \sigma_{xyy}^{(B)}$) which elucidates that $\rho_{xyy}^{(2)}$ also depends on intrinsic band geometric quantities. The NL Hall resistivity $\rho_{xyy}^{(2)}$ decreases with the Fermi energy as shown in Fig. 9(c). The scattering time dependence goes as $\rho_{xyy}^{(2)} \propto 1/\tau$ and the ratio $\rho_{xyy}^{(2)}/\rho_{yy} \propto \tau^0$. We notice that the ratio $\rho_{xyy}^{(2)}/\rho_{yy}$ decreases with the Fermi energy and δ_0 . We emphasize that the NL longitudinal resistivities $\rho_{xxx}^{(2)} \propto B$ whereas $\rho_{yyy}^{(2)}$ vanishes in the system due to the surviving mirror symmetry along the x -direction.

V. CONCLUSIONS

In this work, we have studied the linear and second-order nonlinear current responses of a 2D gapped semi-Dirac system with merging Dirac nodes in the presence of a weak magnetic field using semiclassical Boltzmann formalism. In particular, we discussed the contribution of Berry curvature and OMM to the linear and NL magnetoconductivities. The nonzero components of these different contributions are highlighted in Table I. We have

obtained the exact analytical expression of linear and NL magnetoconductivities of the system in terms of complete elliptic integral of the first and second kind respectively which helped in analyzing the dependence of conductivities on Fermi energy and δ_0 . For $\delta_0 > 0$, the change in Fermi surface topology (single-connected Fermi surface for high Fermi energy and two Fermi surfaces for low Fermi energy) with Fermi energy is also reflected in the behavior of obtained linear and nonlinear conductivities. A small kink is observed at the saddle point $\gamma = 1$ for the fixed positive values of δ_0 which marks the transition between two different type of Fermi surfaces. We obtained the approximate expressions of conductivities for low Fermi energy and explicitly showed their Fermi energy and δ_0 dependence close to the band edge. We find that the geometric mean (ratio) of Drude conductivities along the x and y directions is independent of δ_0 for low (high) doping. We show that the ratio of the anomalous velocity and Lorentz force-induced NL Hall conductivity to the NL anomalous Hall conductivity is independent of δ_0 and inversely related to Fermi energy only. It is to be noted that in a time-reversal symmetric system, nonlinear Drude conductivity vanishes which implies that NL longitudinal magnetoconductivity arises solely due to geometric quantities.

We further study the nonlinear magnetoresistivities of the system for two different orientations of current flow: (1) along x and (2) along y directions. For the current applied along the x -direction, the NL longitudinal resistivity scales linearly with the magnetic field, while NL Hall resistivity is independent of B in the lowest B -order. However, for the current applied along the y -direction, the longitudinal NL resistivity vanishes in both zeroth and linear order of B and NL Hall resistivity varies linearly with B in the lowest order. The predicted B -linear dependence of magnetoresistivity mainly comes from nonlinear conductivities which are nonzero due to band geometric quantities and spectrum anisotropy. Our results provide the platform for understanding the NL magnetotransport induced by geometric quantities in 2D semi-Dirac systems.

ACKNOWLEDGEMENTS

We would like to thank Kamal Das for useful discussions.

- ¹ K. S. Novoselov, A. K. Geim, S. V. Morozov, D. Jiang, Y. Zhang, S.V. Dubonos, I. V. Gregorieva and A. A. Firsov, *Science*, **306**, 666 (2004).
- ² A. H. Castro Neto, F. Guinea, N. M. R. Peres, K. S. Novoselov, and A. K. Geim, *Rev. Mod. Phys.* **81**, 109 (2009).
- ³ A. Kobayashi, S. Katayama, Y. Suzumura, and H. Fukuyama, *J. Phys. Soc. Jpn.* **76**, 034711 (2007).
- ⁴ M. O. Goerbig, J.-N. Fuchs, G. Montambaux, and F. Piéchon, *Phys. Rev. B* **78**, 045415 (2008).
- ⁵ Y. Suzumura and A. Kobayashi, *J. Phys. Soc. Jpn.* **80**, 104701 (2011).
- ⁶ M. Hirata, K. Ishikawa, G. Matsuno, A. Kobayashi, K. Miyagawa, M. Tamura, C. Berthier, and K. Kanoda, *Science* **358**, 1403 (2017).
- ⁷ X. F. Zhou, X. Dong, A. R. Oganov, Q. Zhu, Y. Tian, and H. T. Wang, *Phys. Rev. Lett.* **112**, 085502 (2014).
- ⁸ A. D. Zabolotskiy and Y. E. Lozovik, *Phys. Rev. B* **94**, 165403 (2016).
- ⁹ S. Bittner, B. Dietz, M. Miski-Oglu, P. Oria Iriarte, A. Richter, and F. Schäfer, *Phys. Rev. B* **82**, 014301 (2010).
- ¹⁰ M. Polini, F. Guinea, M. Lewenstein, H. C. Manoharan, and V. Pellegrini, *Nat. Nanotech.* **8**, 625 (2013).
- ¹¹ M. Bellec, U. Kuhl, G. Montambaux, and F. Mortessagne, *Phys. Rev. Lett.* **110**, 033902 (2013).
- ¹² T. Jacqmin, I. Carusotto, I. Sagnes, M. Abbarchi, D. D. Solnyshkov, G. Malpuech, E. Galopin, A. Lemaître, J. Bloch, and A. Amo, *Phys. Rev. Lett.* **112**, 116402 (2014).
- ¹³ S.-L. Zhu, B. Wang and L.-M. Duan, *Phys. Rev. Lett.* **98**, 260402 (2007).
- ¹⁴ J.-M. Hou, W.-X. Yang and X.-J. Liu, *Phys. Rev. A* **79**, 043621 (2009).
- ¹⁵ B. Wunsch, F. Guinea, and F. Sols, *New J. Phys.* **10**, 103027 (2008).
- ¹⁶ Y. Hasegawa, R. Konno, H. Nakano, and M. Kohmoto, *Phys. Rev. B* **74**, 033413 (2006).
- ¹⁷ G. Montambaux, F. Piéchon, J.-N. Fuchs, and M. O. Goerbig, *Phys. Rev. B* **80**, 153412 (2009).
- ¹⁸ G. Montambaux, F. Piéchon, J.-N. Fuchs, and M. O. Goerbig, *Eur. Phys. J. B* **72**, 509 (2009).
- ¹⁹ V. Pardo, and W. E. Pickett, *Phys. Rev. Lett.* **102**, 166803 (2009).
- ²⁰ Y. Wu, *Opt. Express* **22**, 1906 (2014).
- ²¹ L. Tarruell, D. Greif, T. Uehlinger, G. Jotzu, and T. Esslinger, *Nature* **483**, 10871 (2012).
- ²² P. Adroguier, D. Carpentier, G. Montambaux and E. Orignac, *Phys. Rev. B* **93**, 125113 (2016).
- ²³ A. Mawrie and B. Muralidharan, *Phys. Rev. B* **99**, 075415 (2019).
- ²⁴ J. P. Carbotte and E. J. Nicol, *Phys. Rev. B* **100**, 035441 (2019).
- ²⁵ J. Jang, S. Ahn, and H. Min, *2D Materials* **6**, 025029 (2019).
- ²⁶ D. O. Oriekhov, V. P. Gusynin, arXiv:2206.14558.
- ²⁷ P. Dietl, F. Piéchon, and G. Montambaux, *Phys. Rev. Lett.* **100**, 236405 (2008).
- ²⁸ P. Delplace, and G. Montambaux, *Phys. Rev. B* **82**, 035438 (2010).
- ²⁹ X. Zhou, W. Chen, and X. Zhu, *Phys. Rev. B* **104**, 235403 (2021).
- ³⁰ P. K. Pyatkovskiy and T. Chakraborty, *Phys. Rev. B* **93**, 085145 (2018).
- ³¹ P. Sinha, S. Murakami and S. Basu, *Phys. Rev. B* **102**, 085416 (2020).
- ³² K. Saha, *Phys. Rev. B* **94**, 081103(R) (2016).
- ³³ S. Mondal and S. Basu, *Phys. Rev. B* **105**, 235441 (2022).
- ³⁴ D. Xiao, M.-C. Chang, and Q. Niu, *Rev. Mod. Phys.* **82**, 1959 (2010).
- ³⁵ F. D. M. Haldane, *Phys. Rev. Lett.* **93**, 206602 (2004).
- ³⁶ N. A. Sinitsyn, *Journal of Physics: Condensed Matter* **20**, 023201 (2008).
- ³⁷ A. A. Burkov and L. Balents, *Phys. Rev. Lett.* **107**, 127205, (2011).
- ³⁸ T. Qin, Q. Niu and J. Shi, *Phys. Rev. Lett.* **107**, 236601 (2011).
- ³⁹ P. Goswami and S. Tewari, *Phys. Rev. B* **88**, 245107 (2013).
- ⁴⁰ S. Nandy, G. Sharma, A. Taraphder and S. Tewari, *Phys. Rev. Lett.* **119**, 176804 (2017).
- ⁴¹ A. A. Burkov, *Phys. Rev. B* **96**, 041110 (2017).
- ⁴² K.-S. Kim, H.-J. Kim and M. Sasaki, *Phys. Rev. B* **89**, 195137 (2014).
- ⁴³ H. Zhou, C. Xiao, and Q. Niu, *Phys. Rev. B* **100**, 041406 (2019).
- ⁴⁴ I. Sodemann and L. Fu, *Phys. Rev. Lett.* **115**, 216806 (2015).
- ⁴⁵ C. Xiao, Z. Z. Du, and Q. Niu, *Phys. Rev. B* **100**, 165422 (2019).
- ⁴⁶ K. Kang, T. Li, E. Sohn, J. Shan, and K. F. Mak, *Nature Materials* **18**, 324-328 (2019).
- ⁴⁷ J. Son, K.-H. Kim, Y. H. Ahn, H.-W. Lee, and J. Lee, *Phys. Rev. Lett.* **123**, 036806 (2019).
- ⁴⁸ Y. Zhang, Y. Sun, and B. Yan, *Phys. Rev. B* **97**, 041101 (2018).
- ⁴⁹ Z. Z. Du, C. M. Wang, H.-Z. Lu, and X. C. Xie, *Phys. Rev. Lett.* **121**, 266601 (2018).
- ⁵⁰ J. I. Facio, D. Efremov, K. Koepernik, J.-S. You, I. Sodemann, and J. van den Brink, *Phys. Rev. Lett.* **121**, 246403 (2018).
- ⁵¹ Z. Z. Du, C. M. Wang, S. Li, H.-Z. Lu, and X. C. Xie, *Nature Communications* **10**, 3047 (2019).
- ⁵² B. T. Zhou, C.-P. Zhang, and K. Law, *Phys. Rev. Applied* **13**, 024053 (2020).
- ⁵³ Z. Z. Du, C. M. Wang, H.-P. Sun, H.-Z. Lu, and X. C. Xie, *Nature Communications* **12**, 5038 (2021).
- ⁵⁴ R. Battilomo, N. Scopigno, and C. Ortix, *Phys. Rev. Lett.* **123**, 196403 (2019).
- ⁵⁵ S. S. Samal, S. Nandy, and K. Saha, *Phys. Rev. B* **103**, L201202 (2021).
- ⁵⁶ G. Sundaram and Q. Niu, *Phys. Rev. B* **59**, 14915 (1999).
- ⁵⁷ T. Morimoto, S. Zhong, J. Orenstein and J. E. Moore, *Phys. Rev. B* **94**, 245121 (2016).
- ⁵⁸ M. -C. Chang, and Q. Niu, *Phys. Rev. B* **53**, 7010, (1996).
- ⁵⁹ D. Xiao, W. Yao, and Q. Niu, *Phys. Rev. Lett.* **99**, 236809 (2007).
- ⁶⁰ N. W. Ashcroft and N. D. Mermin, *Solid State Physics, HRW International Editions* (Holt, Rinehart and Winston, New York, 1976).
- ⁶¹ J. M. Ziman, *Electrons and Phonons: The Theory of Transport Phenomena in Solids* (Clarendon Press, Oxford, 1967).
- ⁶² H. K. Pal and D. L. Maslov, *Phys. Rev. B* **81**, 214438

- (2010).
- ⁶³ Q. Ma, S.-Y. Xu, H. Shen, D. MacNeill, V. Fatemi, T.-R. Chang, A. M. Mier Valdivia, S. Wu, Z. Du, C.-H. Hsu, S. Fang, Q. D. Gibson, K. Watanabe, T. Taniguchi, R. J. Cava, E. Kaxiras, H.-Z. Lu, H. Lin, L. Fu, N. Gedik, and P. Jarillo-Herrero, *Nature* **565**, 337 (2019).
 - ⁶⁴ S. Lahiri, T. Bhore, K. Das, and A. Agarwal, *Phys. Rev. B* **105**, 045421 (2022).
 - ⁶⁵ P. He, S. S.-L. Zhang, D. Zhu, Y. Liu, Y. Wang, J. Yu, G. Vignale, and H. Yang, *Nat. Phys.* **14**, 495 (2018).
 - ⁶⁶ P. He, S. S.-L. Zhang, D. Zhu, S. Shi, O. G. Heinonen, G. Vignale, and H. Yang, *Phys. Rev. Lett.* **123**, 016801 (2019).